Supplementary Information for

The physics of pencil drawing

Aubin Archambault,[1] Lucie Domino,[1] and Vincent Bertin[1,2,*]

[1] *Aix Marseille Univ, CNRS, IUSTI UMR 7343, Marseille 13453, France*

[2] *Université Côte d'Azur, CNRS, INPHYNI UMR 7010, Nice 06200, France*

(Dated: November 18, 2026)

* vincent.bertin@univ-cotedazur.fr

CONTENTS

S1. Mechanical characterization of the pencil leads 3

S2. Determination of the transferred volume 5

S3. Optical image segmentation 6

S4. Debris-area statistics 7

S4.1. Construction of the debris-area probability density 7

S4.2. Determination of the experimental scaling exponent 8

S5. Contact-patch statistics of self-affine rough surfaces 11

S5.1. Dependence on spectral bandwidth 11

S5.2. Dependence on relative real contact area 13

S5.3. Relation to Mandelbrot number–area scaling 14

S6. Dependence of surface coverage on load and pencil hardness 14

References 16

S1. MECHANICAL CHARACTERIZATION OF THE PENCIL LEADS

The mechanical properties of the pencil leads were characterized using a Hysitron TI Premier nanoindenter equipped with a Berkovich TI 0039 diamond tip. For each pencil grade, 16 indentations were performed on a 4×4 grid with a spacing of $15\,\mu$m. Different maximum loads were imposed, resulting in indentation depths ranging approximately from 100 nm to $2.5\,\mu$m. The spacing between indentations was large enough compared with their lateral dimensions, so that neighboring measurements did not interact.

The hardness σ_p and reduced elastic modulus E^* were determined from the measured load–displacement curves using standard instrumented-indentation analysis. The unloading branch was fitted by a power law, from which the initial unloading stiffness S was determined. The contact depth and calibrated projected contact area A_c of the Berkovich tip were then evaluated, giving

$$\sigma_p = \frac{F_{\max}}{A_c}, \qquad E^* = \frac{\sqrt{\pi}}{2}\frac{S}{\sqrt{A_c}}, \tag{S1}$$

where the calibrated tip-area function was used rather than the ideal Berkovich geometry. For reference, an ideal Berkovich indenter has a projected contact area $A_c \simeq 24.5h_c^2$, such that a contact depth of 200 nm corresponds to an equivalent contact diameter of approximately $1.1\,\mu$m.

All individual load–displacement curves were inspected before calculating the mechanical properties of each pencil grade. Measurements exhibiting clear curve-level artefacts were discarded. The most common identifiable artefact was an incorrect determination of the initial surface-contact position, leading to anomalously large apparent indentation depths of several micrometres compared with measurements performed under similar loading conditions. Other measurements were discarded only when the load–displacement curve itself showed a clearly anomalous response that prevented a reliable indentation analysis. The resulting value of σ_p or E^* was not used as an exclusion criterion. Between 12 and 15 of the 16 initial measurements were retained for each grade.

Supplementary Fig. S1(a) shows the 15 (out of 16) retained load–displacement curves for the HB pencil lead. The corresponding hardness values are plotted against the imposed maximum load in Supplementary Fig. S1(b). Considerable position-to-position variability remains among the retained measurements, but no systematic dependence of hardness on maximum load is observed over the explored range. Across the seven grades, the standard

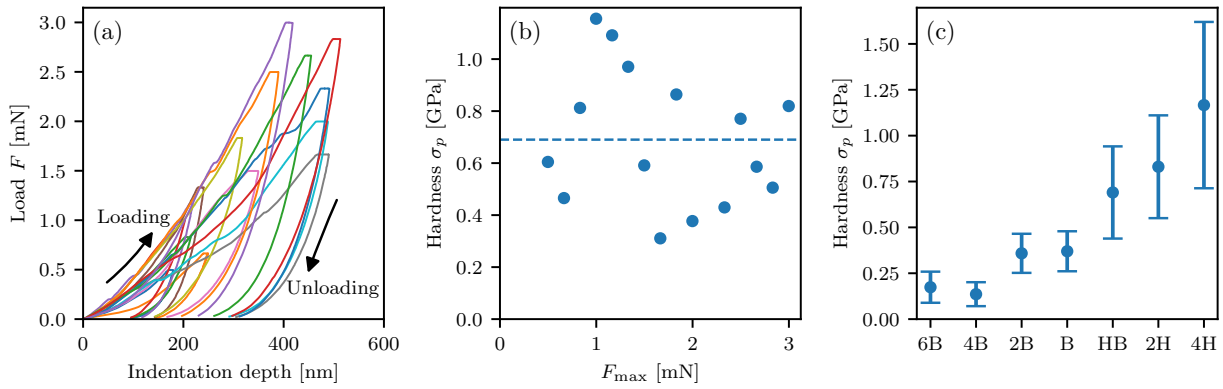


FIG. S1. **Mechanical characterization of the graphite–clay pencil leads.** (a) Load–displacement curves for the 15 retained indentations performed on the HB pencil lead. Different maximum loads were imposed to probe the mechanical response over a range of indentation depths. The arrows indicate the loading and unloading branches. (b) Hardness σ_p obtained from the retained HB indentations as a function of the maximum indentation load $F_{\max}$. The horizontal dashed line indicates the mean hardness. Despite substantial position-to-position variability, no systematic dependence of σ_p on $F_{\max}$ is observed over the explored range. (c) Mean hardness σ_p for the seven pencil grades, from 6B to 4H. Error bars indicate one standard deviation among the retained individual indentations. For each grade, 16 indentations were initially performed, of which 12–15 were retained after inspection of the load–displacement curves.

deviation of the individual hardness measurements represents approximately 29–49% of the corresponding mean value.

This dispersion should not be interpreted simply as instrumental uncertainty on a single homogeneous material property. Each indentation probes a different micrometric region of the heterogeneous graphite–clay lead, and the observed scatter may therefore reflect genuine spatial variations in local composition and microstructure. The rough, non-planar surface of the leads and the associated local contact geometry may also contribute. We do not attempt to separate these contributions.

Supplementary Fig. S1(c) reports the mean hardness and standard deviation of the retained measurements for all seven grades. The error bars therefore quantify the local position-to-position variability within each pencil lead rather than the uncertainty on the grade-averaged hardness. Throughout the main-text analysis, each grade is characterized

by the mean value of σ_p obtained from the retained indentations.

S2. DETERMINATION OF THE TRANSFERRED VOLUME

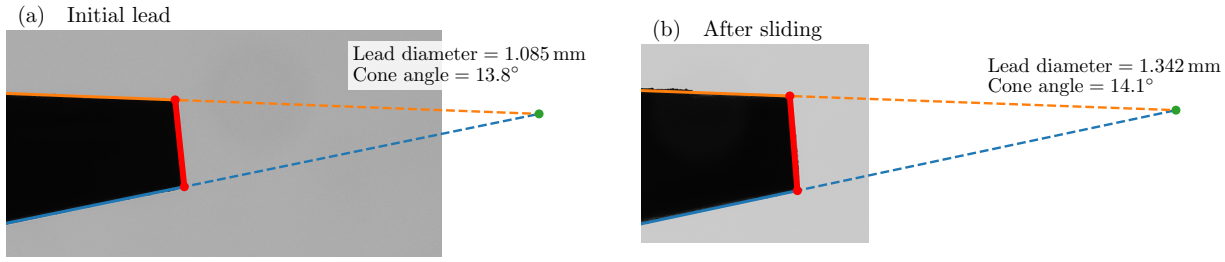


FIG. S2. **Determination of the transferred volume from the pencil-tip geometry.** Side-view images of the pencil tip (a) before and (b) after sliding. Solid lines indicate the detected lateral edges of the conical tip, while dashed lines show their extrapolation to the virtual cone apex. The red segment indicates the detected diameter of the flat lead end. The lead diameter and cone opening angle extracted from each image are reported in the panels and are used to reconstruct the removed volume assuming a conical tip geometry.

The volume of material removed from the pencil was determined from side-view images of the pencil tip acquired before and after sliding. The two lateral edges of the conical tip and the flat worn end were detected using a Canny edge detector followed by Hough-line transforms (Fig. S2). The intersections of the flat-end line with the two lateral edges define the lead diameter d, while the angle between the two lateral edges provides the full cone opening angle Θ. Assuming a conical geometry, the volume extending from the virtual cone apex to a section of diameter d is

$$V(d, \Theta) = \frac{\pi d^3}{24 \tan(\Theta/2)}. \tag{S2}$$

The removed volume is obtained as the difference between the volumes reconstructed from the final and initial images. The opening angle typically increases slightly between the initial and final images (Fig. S2), revealing a small departure from a perfectly conical geometry. We therefore calculate the transferred volume using the mean opening angle, $\bar{\Theta} = (\Theta_{\text{initial}} + \Theta_{\text{final}})/2$, and estimate its uncertainty as $|\Delta V(\Theta_{\text{initial}}) - \Delta V(\Theta_{\text{final}})|$. With this criterion, the transferred-volume uncertainty is typically $\pm 15\%$, with a range of approximately ± 6–30%.

S3. OPTICAL IMAGE SEGMENTATION

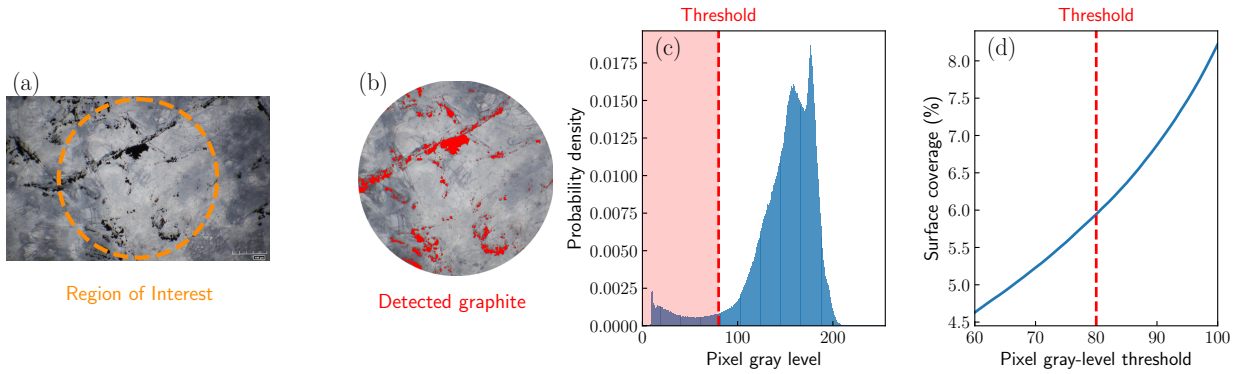


FIG. S3. **Determination and threshold sensitivity of graphite surface coverage.** (a) Representative optical microscopy image showing the circular region of interest used for the analysis. The peripheral region is excluded because the illumination intensity decreases near the edges of the microscope field of view. (b) Pixels identified as graphite using the prescribed grayscale threshold 80. (c) Distribution of grayscale pixel intensities within the region of interest. The shaded region corresponds to pixels classified as graphite for the threshold value 80. (d) Surface coverage measured for the same image as a function of the grayscale threshold. The dashed red line indicates the value 80 used in the analysis.

The graphite surface coverage is determined from optical microscopy images using intensity thresholding, as illustrated in Fig. S3. Each image is first converted to grayscale. Because the illumination intensity decreases near the edges of the field of view due to the optical response of the microscope objective, a circular region of interest centered on the image is used to exclude these peripheral regions and retain an approximately uniform illumination.

Within this region, pixels with a gray level below a prescribed threshold are classified as graphite (Fig. S3(b)). The gray-level distribution is broad and does not exhibit a sharp separation between graphite and the paper background (Fig. S3(c)), so that the appropriate threshold is not uniquely defined by the intensity histogram alone. We therefore selected a threshold value of 80 based on visual inspection of the segmented images. As an independent check, applying the same threshold to graphite-free paper imaged under identical conditions gives an apparent surface coverage below 0.1%, indicating that only a very small fraction of the bare substrate is incorrectly classified as graphite.

We also tested automatic global-thresholding procedures. Because of the broad distribution of gray levels associated with the paper substrate, these methods frequently selected thresholds that extended into the background-intensity distribution and consequently classified substantial regions of bare paper as graphite. We therefore retained the fixed manually selected threshold and applied it consistently to all images acquired under the same illumination conditions.

The surface coverage ϕ used in Fig. 4 of the manuscript is then defined as the fraction of pixels classified as graphite within the region of interest,

$$\phi = \frac{N_{\mathrm{graphite}}}{N_{\mathrm{ROI}}}, \tag{S3}$$

where N_{graphite} is the number of pixels below the threshold and N_{ROI} is the total number of pixels within the region of interest. Illumination conditions were kept fixed within each experimental dataset, and the same intensity threshold was applied to all corresponding images.

To assess the sensitivity of the segmentation procedure, we varied the gray-level threshold between 60 and 100 for the representative image shown in Fig. S3(d). The resulting surface coverage varies smoothly with threshold, from approximately 4.6% to 8.2%. Around the value 80 used in the analysis, changing the threshold by ± 10 modifies the measured surface coverage by only about 10–15%.

For each experimental condition, eight micrographs were acquired at different positions along the same drawing trace. The surface coverage reported in Fig. 4(c) of the main text and below (Sec. S6) is the mean over these eight fields of view, while the corresponding standard deviation characterizes the spatial variability of the deposited graphite along the trace.

S4. DEBRIS-AREA STATISTICS

S4.1. Construction of the debris-area probability density

For each pencil grade and applied normal load, eight optical micrographs were acquired at different positions along the same drawing trace. The images were converted to grayscale and analyzed within the circular region of interest described in Sec. S3. Graphite pixels were identified using the same prescribed intensity threshold, and connected regions of graphite

pixels were identified as individual transferred patches using eight-neighbour connectivity. The area $\mathcal{A}$ of each patch was obtained from its number of pixels using the microscope calibration, corresponding to a pixel size of approximately $0.40\,\mu$m and hence a pixel area $\mathcal{A}_{\mathrm{pix}} \simeq 0.16\,\mu\mathrm{m}^2$.

For each experimental condition, all connected graphite patches detected within the eight fields of view were pooled to construct the debris-area probability density. No smoothing or averaging of the probability density was performed. The distribution was evaluated using logarithmically spaced area bins. For a bin i containing N_i patches and spanning an interval of width $\Delta\mathcal{A}_i$, the probability density is calculated as

$$P_i = \frac{N_i}{N_{\mathrm{tot}}\Delta\mathcal{A}_i}, \tag{S4}$$

where N_{tot} is the total number of patches detected for that experimental condition.

At small areas, the measured patch area is discrete, $\mathcal{A} = n\mathcal{A}_{\mathrm{pix}}$, where $n \in \mathbb{N}$ is the number of pixels in a connected patch. Because logarithmic bin boundaries do not generally coincide with these discrete admissible areas, bins approaching the pixel scale contain only a small number of possible patch sizes, or can contain none at all. This produces the characteristic binning-dependent structure observed at the lower end of the distributions. To exclude this pixel-discretization regime, quantitative fits are restricted to $\mathcal{A} \geq \mathcal{A}_{\mathrm{fit,min}} = 2\,\mu\mathrm{m}^2$.

S4.2. Determination of the experimental scaling exponent

The compact representation used in Fig. 3(a) of the manuscript emphasizes the similarity between the debris-area distributions and shows that an approximate $\mathcal{A}^{-3/2}$ scaling provides a useful common description. Here, we examine this scaling more quantitatively by determining the exponent separately for each pencil grade. Figure S4(a) shows the five grades for which a sufficiently extended intermediate scaling regime is resolved, with the distributions vertically shifted for clarity and the individual power-law fits shown explicitly.

The two hardest grades, 4H and 2H, exhibit substantially smaller upper cutoffs and consequently do not provide a sufficiently extended intermediate regime for a meaningful individual determination of τ. They are therefore shown in Fig. 3(a) of the main text but excluded from the quantitative exponent analysis presented here.

For reference, the total numbers of detected patches in the measurements shown in

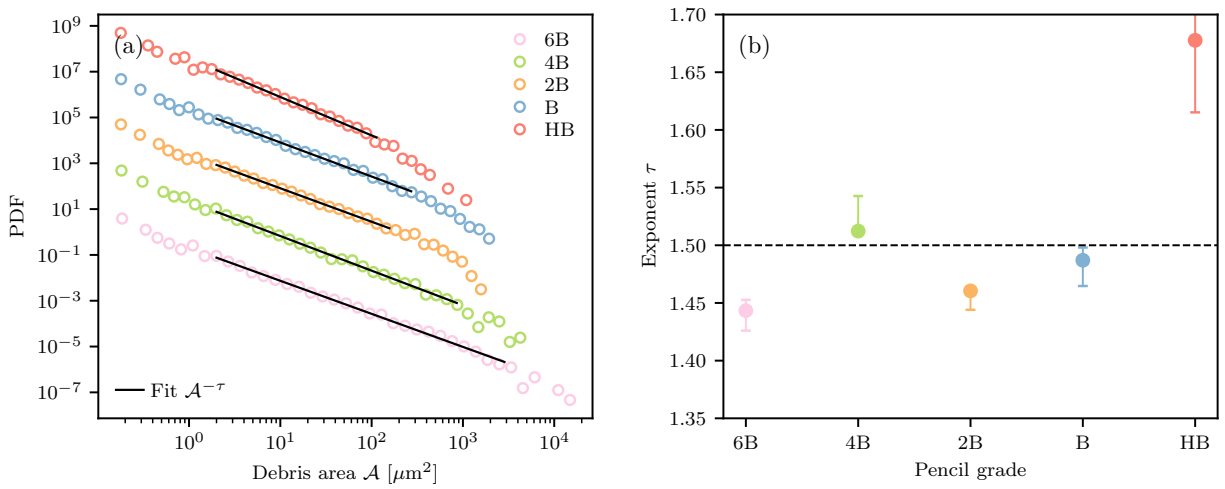


FIG. S4. **Grade dependence of the debris-area scaling exponent.** (a) Probability density $P(\mathcal{A})$ of connected graphite-patch areas for the five pencil grades HB–6B at $F_N = 1.8\,\mathrm{N}$. The distributions are vertically shifted for clarity. Black lines show individual power-law fits, $P(\mathcal{A}) \propto \mathcal{A}^{-\tau}$, over the intermediate scaling regime. The common lower fitting bound is $\mathcal{A}_{\mathrm{fit,min}} = 2\,\mu\mathrm{m}^2$. For each grade, the upper fitting bound is determined independently as $\mathcal{A}_{\mathrm{fit,max}} = 0.3\mathcal{A}_c$, where $\mathcal{A}_c$ is obtained from a preliminary truncated-power-law fit. (b) Fitted exponent τ as a function of pencil grade. The dashed horizontal line indicates $\tau = 3/2$. Error bars in (b) show the variation obtained when the upper fitting bound is varied from $0.2\mathcal{A}_c$ to $0.4\mathcal{A}_c$.

Fig. 3(a) are 5453, 8066, 16161, 8248, 8431, 7263, and 4831 for 4H, 2H, HB, B, 2B, 4B, and 6B, respectively. Despite these large sample sizes, the probability densities are not perfectly smooth. Point-to-point fluctuations remain visible around the approximate power-law behaviour, while at the largest patch areas the progressively smaller number of detected objects produces stronger finite-count fluctuations and a systematic departure from the algebraic regime toward a grade-dependent cutoff.

At small areas, all fits are restricted to

$$\mathcal{A} \geq \mathcal{A}_{\mathrm{fit,min}} = 2\,\mu\mathrm{m}^2, \tag{S5}$$

as discussed above, in order to exclude the pixel-discretization regime. At large areas, each distribution progressively departs from an algebraic form and develops a grade-dependent cutoff. Because the position of this cutoff varies substantially between grades, the upper bound of the power-law fit is determined independently for each distribution.

We first fit each debris-area distribution to a truncated power law,

$$P(\mathcal{A}) = C\,\mathcal{A}^{-\tau_{\mathrm{cut}}} \exp\left(-\frac{\mathcal{A}}{\mathcal{A}_c}\right), \tag{S6}$$

where $\mathcal{A}_c$ defines the characteristic area of the large-area cutoff. This preliminary fit is used only to determine the cutoff scale $\mathcal{A}_c$ and the resulting exponent τ_{cut} is not used in the subsequent scaling analysis.

The final scaling exponent τ is then determined from a pure power-law fit,

$$P(\mathcal{A}) = C'\mathcal{A}^{-\tau}, \tag{S7}$$

over the interval

$$2\,\mu\mathrm{m}^2 \le \mathcal{A} \le \mathcal{A}_{\mathrm{fit,max}}, \qquad \mathcal{A}_{\mathrm{fit,max}} = 0.3\mathcal{A}_c. \tag{S8}$$

This procedure provides a grade-dependent upper fitting bound while applying the same criterion to all five distributions. The corresponding fitting intervals are shown directly by the black fit segments in Fig. S4(a).

The resulting individual exponents vary from $\tau \simeq 1.44$ to $\tau \simeq 1.51$ for B–6B, while the HB pencil gives a somewhat larger value, $\tau \simeq 1.68$. Thus, the five distributions do not share an exactly identical exponent, but their fitted values remain clustered around $\tau = 3/2$ (Fig. S4(b)). Because the fitted exponent is more sensitive to the choice of the fitting interval than to the statistical uncertainty of the regression itself, we estimate its uncertainty from the sensitivity to the upper fitting bound. The error bars shown in Fig. S4(b) are obtained by varying the upper fitting bound from $0.2\mathcal{A}_c$ to $0.4\mathcal{A}_c$, around the reference choice $\mathcal{A}_{\mathrm{fit,max}} = 0.3\mathcal{A}_c$.

For comparison with the compact representation used in the main text, we also perform a global fit of the HB–6B distributions over the common interval

$$2\,\mu\mathrm{m}^2 \le \mathcal{A} \le 100\,\mu\mathrm{m}^2. \tag{S9}$$

Fitting a single exponent to all retained probability-density points gives

$$\tau = 1.489 \pm 0.017. \tag{S10}$$

The global exponent is therefore very close to 3/2 and provides a convenient single-value description of the experimentally observed scaling regime. The individual fits nevertheless show that 3/2 should be regarded as an approximate common scaling exponent rather than an exact grade-independent value.

S5. CONTACT-PATCH STATISTICS OF SELF-AFFINE ROUGH SURFACES

The bearing-area model reproduces remarkably well the qualitative features of the experimentally measured debris-area distributions: the contact-patch statistics display a broad power-law regime with an exponent close to 3/2, together with a large-area cutoff that shifts with the relative contact area. We now examine more quantitatively how the fitted exponent depends on the parameters controlling the contact-patch statistics.

The scaling analysis is restricted to the intermediate range of contact-patch areas,

$$\lambda_{\min}^2 \ll A \ll \lambda_{\max}^2, \tag{S11}$$

away from the short- and long-wavelength spectral cutoffs. Within this regime, the absolute position of the self-affine interval does not affect the fitted exponent within numerical accuracy; what matters is the extent of the available scale separation. For a fixed Hurst exponent H, the contact-patch statistics are therefore controlled by two main dimensionless parameters: the extent of the self-affine spectral range and the relative real contact area. We quantify the former by

$$n = \log_{10}\left(\frac{\lambda_{\max}}{\lambda_{\min}}\right), \tag{S12}$$

and the latter by

$$\frac{A_{\mathrm{real}}}{A_0} = \frac{F_N}{\sigma_p L_0^2}. \tag{S13}$$

We repeat the bearing-area simulations used in Fig. 3(b), varying these two parameters independently while keeping $H = 0.5$. For each condition, contact-patch areas are pooled over 100 independent surface realizations to construct $P(A)$, typically yielding between 2×10^5 and 5×10^5 individual contact patches. The exponent τ is then determined from the resulting distribution within the intermediate scaling regime.

S5.1. Dependence on spectral bandwidth

We first vary the spectral bandwidth n at fixed relative real contact area $A_{\mathrm{real}}/A_0 = 0.1$. Figure S5(a) shows representative contact-patch area distributions for $n = 1.5$, 2, 2.5, and 3. In all cases, the distributions exhibit an intermediate approximately algebraic regime, followed by a large-area cutoff. As the spectral bandwidth increases, this scaling regime progressively extends over a broader range of patch areas.

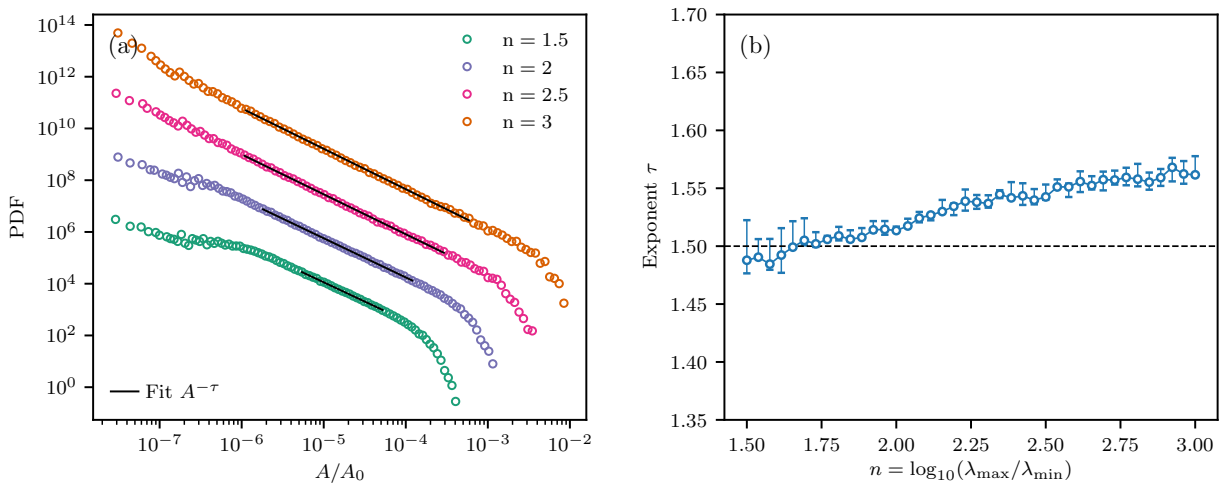


FIG. S5. **Dependence of contact-patch statistics on spectral bandwidth.** (a) Probability density of connected contact-patch areas for self-affine surfaces with $H = 0.5$ and spectral bandwidths $n = \log_{10}(\lambda_{max}/\lambda_{min}) = 1.5$, 2, 2.5, and 3, at fixed relative real contact area $A_{real}/A_0 = 0.1$. The distributions are vertically shifted for clarity; black lines show the power-law fits $P(A) \propto A^{-\tau}$ over the retained fitting intervals. (b) Fitted exponent τ as a function of spectral bandwidth n. Error bars quantify the sensitivity to the fitting interval, and the horizontal dashed line indicates $\tau = 3/2$.

To quantify the scaling exponent, we fit the intermediate part of each distribution to $P(A) \propto A^{-\tau}$. We choose the lower fitting bound $A_{fit,min}$ to satisfy two requirements: (i) it corresponds to at least ~ 20 pixels, to avoid pixel-discretization effects, and (ii) it lies above the shortest self-affine scale, $A_{fit,min} \geq (2\lambda_{min})^2$. The upper fitting bound follows the same criterion as for the experimental debris distributions (Sec. S4.2), namely $A_{fit,max} = 0.3A_c$, with the uncertainty estimated by varying this bound between $0.2A_c$ and $0.4A_c$.

The fitted exponent remains close to 3/2 over the whole range investigated, but displays a weak systematic dependence on spectral bandwidth (Fig. S5(b)). It increases from approximately $\tau \simeq 1.49$ for $n = 1.5$ to $\tau \simeq 1.56$–1.57 for $n = 3$. The larger uncertainty at the smallest bandwidths reflects the shorter scaling range available for fitting.

These results show that the contact-patch exponent is not strictly independent of the extent of the self-affine roughness spectrum. Nevertheless, over the range of spectral bandwidths accessible here, its variation remains modest and the distributions are consistently characterized by an exponent of order 3/2.

S5.2. Dependence on relative real contact area

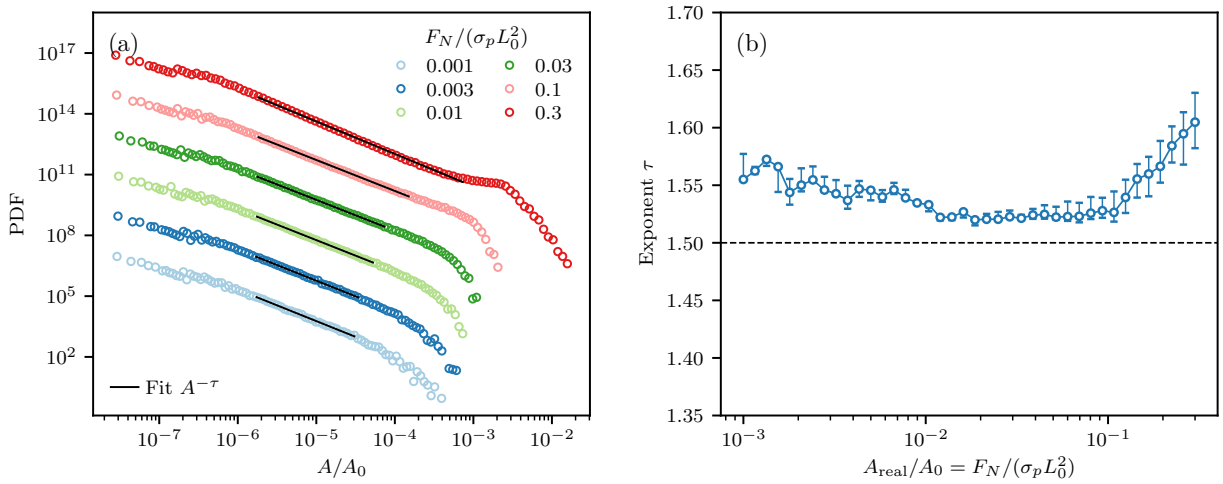


FIG. S6. **Dependence of contact-patch statistics on relative real contact area.** (a) Probability density of connected contact-patch areas for self-affine surfaces with $H = 0.5$ and $n = 2$, for the same relative real contact areas A_{real}/A_0 as in Fig. 3(b). The distributions are vertically shifted for clarity; black lines show the power-law fits $P(A) \propto A^{-\tau}$. (b) Fitted exponent τ as a function of relative real contact area. The fitting procedure and error bars are defined as in the previous section, and the horizontal dashed line indicates $\tau = 3/2$.

We next keep the spectral bandwidth fixed at $n = 2$, as in Fig. 3(b), and vary the relative real contact area over the same values, $A_{\mathrm{real}}/A_0 = 0.001$, 0.003, 0.01, 0.03, 0.1, and 0.3. The corresponding contact-patch distributions are shown in Fig. S6(a). Increasing the contact fraction shifts the large-area cutoff towards larger patches, while preserving an extended approximately algebraic regime.

The fitted exponent shows a weak but non-monotonic dependence on contact fraction (Fig. S6(b)). Over the sparse- and intermediate-contact regime, τ remains close to 3/2, decreasing from approximately 1.55–1.56 at the lowest contact fractions to about 1.52 at intermediate values. At larger contact fractions, the system approaches the percolation regime: individual patches increasingly coalesce into large connected clusters, and the area distribution develops a distinct large-A shoulder that is absent far from percolation. Correspondingly, the fitted exponent increases more strongly, reaching approximately $\tau \simeq 1.60$ at $A_{\mathrm{real}}/A_0 = 0.3$.

The experiments span $A_{\mathrm{real}}/A_0 \simeq 0.0016$–$0.043$, and therefore lie within the regime where the exponent remains close to 3/2 and varies only moderately with contact fraction.

S5.3. Relation to Mandelbrot number–area scaling

Lastly, a useful theoretical comparison comes from Mandelbrot's scaling argument for the number–area statistics of geographical islands generated by self-affine geometry. This argument predicts $P(A) \propto A^{-(2-H/2)}$, corresponding to $\tau = 1.75$ for $H = 0.5$ in the asymptotic limit of an infinitely broad self-affine range, $n \to \infty$ [1]. Our simulations over finite spectral bandwidths do not show evidence for such an asymptotic regime: instead, τ remains close to 3/2 and varies weakly with both spectral bandwidth and contact fraction. Numerical studies of thresholded self-affine surfaces have similarly found that the island-area exponent depends on the height threshold, or equivalently on the occupied area fraction, rather than being fixed solely by H [2]. Thus, the exponent of order 3/2 observed here should be regarded as an effective exponent for the finite-bandwidth, finite-contact regime relevant to the experiments, rather than as a universal asymptotic value.

S6. DEPENDENCE OF SURFACE COVERAGE ON LOAD AND PENCIL HARDNESS

In Fig. 4(c) of the main text, the graphite surface coverage is compared with the estimated relative real contact area, $A_{\mathrm{real}}/A_0 \simeq F_N/(\sigma_p A_0)$. This representation combines variations in normal force, pencil hardness and nominal contact area into a single contact-mechanical variable. While useful as a compact representation of the overall dataset, pooling the different pencil grades and loads can obscure their individual dependences. We therefore first examine the effects of normal force at fixed pencil grade and of hardness at fixed load, before returning to the contact-area representation and assessing its range of validity.

At fixed pencil grade, the dependence of surface coverage on normal force varies markedly between grades (Fig. S7(a)). Power-law regressions of the form $\phi \propto F_N^{\alpha}$ yield $\alpha = -0.02 \pm 0.03$ (4H), 0.04 ± 0.19 (2H), 0.71 ± 0.18 (HB), 0.34 ± 0.08 (B), 0.35 ± 0.19 (2B), 1.02 ± 0.13 (4B), and 0.78 ± 0.17 (6B). The coverage is therefore essentially independent of load for the two hardest pencils, whereas substantially stronger load dependences are observed for the

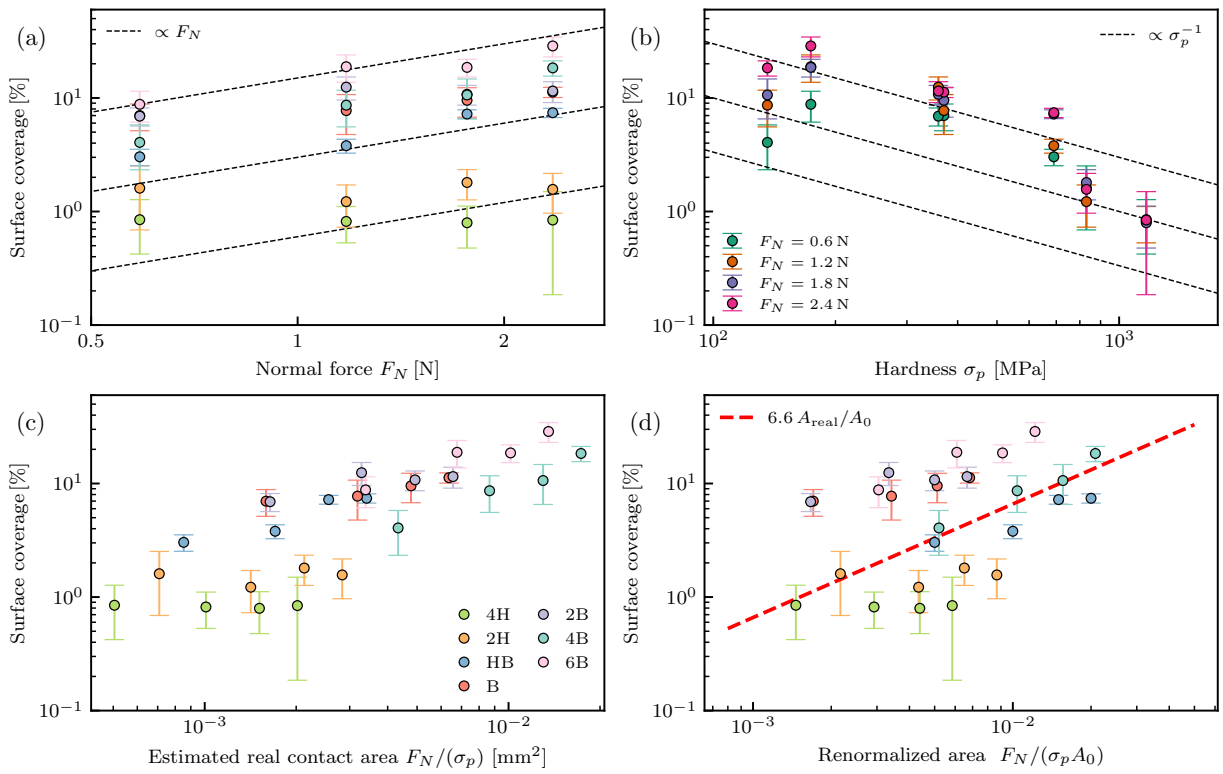


FIG. S7. **Dependence of graphite surface coverage on normal load and pencil hardness.** (a) Surface coverage ϕ as a function of the applied normal force F_N for the different pencil grades. Dashed lines indicate the reference scaling $\phi \propto F_N$ and are shown as guides to the eye. (b) Surface coverage as a function of the mean indentation hardness σ_p at fixed normal force. Dashed lines indicate the reference scaling $\phi \propto \sigma_p^{-1}$. (c) Surface coverage as a function of the estimated real contact area, $A_{\mathrm{real}} \simeq F_N/\sigma_p$. (d) Surface coverage as a function of the estimated relative real contact area, $A_{\mathrm{real}}/A_0 \simeq F_N/(\sigma_p A_0)$, where A_0 is the nominal lead–paper contact area. The red dashed line shows the empirical relation $\phi = 6.6\,A_{\mathrm{real}}/A_0$ as a reference. Error bars indicate one standard deviation across the eight micrographs acquired at different positions along each drawing trace.

softer grades. There is consequently no single load exponent describing all pencil grades.

At fixed normal force, however, the surface coverage decreases systematically as the pencil hardness increases (Fig. S7(b)). Fits of the form $\phi \propto \sigma_p^{\beta}$ give $\beta = -0.84 \pm 0.30$, -1.28 ± 0.33, -1.19 ± 0.34, and -1.46 ± 0.31 for $F_N = 0.6$, 1.2, 1.8, and 2.4 N, respectively. The hardness dependence is therefore consistently strong, with exponents of order -1 over the explored range.

To quantify the combined dependence on load and hardness without imposing the contact-mechanical form, we also fitted all measurements to

$$\phi = C F_N^{\alpha} \sigma_p^{\beta}. \tag{S14}$$

A global least-squares regression in logarithmic variables gives $\alpha = 0.46 \pm 0.21$ and $\beta = -1.20 \pm 0.15$, with $R^2 = 0.73$. The fitted hardness exponent remains close to an inverse dependence, whereas the effective load exponent is substantially smaller than unity. The fitted values provide a compact summary of the overall trends, but also show that the dependence on load is substantially weaker than the simple proportionality expected from F_N/σ_p.

After examining the effects of normal force and hardness separately, we return to the contact-mechanical combinations used in the main text. Figure S7(c) shows the surface coverage as a function of F_N/σ_p, while Fig. S7(d) further normalizes this quantity by the nominal contact area A_0. Both representations organize the overall variation of the measurements, with larger values of F_N/σ_p or $F_N/(\sigma_p A_0)$ generally associated with larger graphite surface coverage. Accounting for the nominal contact area, however, does not produce a substantially improved collapse of the different pencil grades. Significant grade-dependent deviations remain in both representations.

The estimated relative real contact area therefore provides a useful zeroth-order organization of the measurements, but not a quantitative collapse. The empirical relation $\phi = 6.6\, A_{\mathrm{real}}/A_0$ is consequently shown only as a guide to the overall magnitude. The remaining grade-dependent deviations indicate that material properties beyond the mean hardness contribute to fragmentation and transfer, as discussed in the main text.

---

[1] B. B. Mandelbrot, Stochastic models for the Earth's relief, the shape and the fractal dimension of the coastlines, and the number-area rule for islands, Proceedings of the National Academy of Sciences **72**, 3825 (1975).

[2] Z. Olami and R. Zeitak, Scaling of island distributions, percolation, and criticality in contour cuts through wrinkled surfaces, Physical Review Letters **76**, 247 (1996).